

1
2
3 **Guglielmin Mauro^{1*}, Donatelli Marco², Semplice Matteo³, Serra Capizzano Stefano^{2,4}.**

4 1* Department of Theoretical and Applied Sciences, Insubria University, Via Dunant 3, 21100 Varese
5 mauro.guglielmin@uninsubria.it;

6 2 Department of Science and High Technology, Insubria University; 3 Department of Mathematics,
7 University of Turin; 4 Department of Information Technology, Uppsala University.

8 **GROUND SURFACE TEMPERATURE RECONSTRUCTION FOR THE LAST 500 YEARS**
9 **OBTAINED FROM PERMAFROST TEMPERATURES OBSERVED IN THE STELVIO SHARE**
10 **BOREHOLE, ITALIAN ALPS.**

11
12 **ABSTRACT**

13 Here we present the results of the inversion of a multiannual temperature profile (2013, 2014, 2015) of the
14 deepest borehole (235 m) in the mountain permafrost of the world located close to Stelvio Pass in the
15 Central Italian Alps. The Stelvio Share Borehole (SSB) is monitored since 2010 with 13 thermistors placed at
16 different depths between 20 and 235 m. The negligible porosity of the rock (dolostone, < 5%) allows to
17 assume the latent heat effects also negligible. The inversion model here proposed is based on the Tikhonov
18 regularization applied to a discretized heat equation, accompanied by a novel regularizing penalty operator.
19 The general pattern of ground surface temperatures (GST) reconstructed from SSB for the last 500 years
20 are similar to the mean annual air temperature (MAAT) reconstructions for the European Alps. The main
21 difference with respect to MAAT reconstructions relates to post Little Ice Age (LIA) events. Between 1940
22 and 1989, SSB data indicate a cooling of ca 1°C. Subsequently, a rapid and abrupt GST warming (more
23 than 0.8°C per decade) was recorded between 1990 and 2011. This warming is of the same magnitude as
24 the increase of MAAT between 1990 and 2000 recorded in central Europe and roughly doubling the
25 increase of MAAT in the Alps.

26
27 **1 INTRODUCTION**

28 The thermal regime of the uppermost ground is determined by the geothermal heat flow and by the
29 fluctuations of temperature at the surface. If rock was homogeneous and no temperature change were to
30 occur at the surface, the temperature would increase linearly with depth, unless spontaneous heat
31 production is present in the vicinity of the well. The gradient of this temperature increase would be
32 governed solely by the magnitude of the terrestrial heat flow and by the thermal conductivity of the rock.
33 However, variations of ground surface temperature (GST) propagate downwards into the rock as
34 attenuating thermal waves, superimposed on the aforementioned linear temperature profile. The depth to
35 which disturbances can be recorded is determined mainly by the amplitude and duration of the
36 temperature change at the surface. Generally, propagation of climate signals is slow and it can take more
37 than 1,000 years to reach the depth of 500m (Huang et al., 2000). For a better conservation of the climate

38 signal in the thermal profile, no lateral heat advection (due for example to ground water flow) should be
39 present (Lewis and Wang, 1992). Since normally no groundwater circulation is present within continuous
40 permafrost in the polar areas but also in rocky areas within mountain permafrost, boreholes drilled in these
41 areas are particularly suited for GST reconstructions.

42 Lachenbruch and Marshall (1986) were among the first to demonstrate that thermal profiles obtained
43 from boreholes drilled in permafrost can be used to reconstruct ground surface temperature changes.
44 These do not require calibration because the heat conduction equation is directly used to infer
45 temperature changes at the ground surface. Today, the majority of permafrost boreholes used to
46 reconstruct ground surface temperatures are located in the Polar regions of North America and Eurasia
47 where the boreholes can be drilled on flat terrain, with negligible topographical effects, and with a
48 permafrost thicknesses typically exceed 100 m, thereby providing deep temperature logs and long ground
49 surface temperature reconstructions. On the other hand several factors like porosity, water/ice and latent
50 heat flows can influence significantly the thermal properties and the thermal signal especially measured in
51 frozen sediments boreholes as well discussed in Mottaghy and Rath (2006).

52 The Share Stelvio borehole (SSB) in the Italian Alps is the deepest drilled within permafrost in the mid-
53 latitude mountains of Europe. Because the permafrost thickness exceeds 200 m at this site it allows
54 reconstruction of GST for some centuries and much more than in the other mountain permafrost
55 boreholes.. In addition, the Stelvio borehole is located on a rounded summit with gentle side slopes.
56 Therefore, site-specific topographic influences are largely eliminated. As such, it is different to the other
57 boreholes drilled in permafrost in the Alps (e.g. PACE boreholes at Schilthorn or Stockhorn; see Harris et al.,
58 2003; Gruber et al., 2004; Hilbich et al., 2008; Harris et al., 2009).

59 Recent atmospheric warming (over the last century) in the European Alps has been roughly twice the global
60 average (Böhm et al., 2001; Auer et al., 2007). Despite its high sensitivity, no GST reconstruction based on
61 borehole thermal profiles is available for this part of the world. Instead, reconstructions of summer air
62 temperatures have been based on either tree-rings (e.g. Büntgen et al., 2006; Corona et al., 2010) or lake
63 sediments (e.g. Larocque-Tobler et al., 2010; Trachsel et al., 2010) for the last 500-1000 years, or both
64 (Trachsel et al., 2012). With rare exceptions (e.g. ice cores; Barbante et al., 2004), the other proxy data are
65 from sites at elevations that rarely exceed 2000m a.s.l. and all the other monitored permafrost boreholes in
66 Europe do not exceed 100 m of depth (see Harris et al., 2003). However, several papers describe GST
67 reconstructions for the last 500-1000 years using boreholes data at hemispheric or global scales (e.g.
68 Huang et al., 2000; Beltrami and Boulron, 2004).

69 The SSB data provides GST history from a high elevation site (3000 m a.s.l.). Such locations are important
70 because snow cover can affect significantly the GST (Zhang, 2005; Ling and Zhang, 2006; Cook et al., 2008).
71 They are also relevant with respect to glacier dynamics and their feedbacks with the global atmospheric
72 system (IPCC, 2013).

73 This paper reconstructs the ground surface temperatures inferred from this borehole and compares the
74 results with existing multiproxy reconstructions for the European Alps and elsewhere.

75

76 **2 STUDY AREA**

77 The Stelvio–Livrio area is a summer ski location, located between the Stelvio Pass (2758 m a.s.l.) and Mt
78 Livrio (3174 m a.s.l.), within the Stelvio National Park. The area is characterized by bedrock outcrops
79 (mainly dolostone), apart from some Holocene moraines (Figure 1a). The SSB borehole was drilled in 2009
80 and is only 10m from the PACE borehole, drilled in 1998 (46°30'59"N; 10°28'35"E, 3000 m a.s.l., Figure 1b).
81 Both boreholes are located on a flat barren summit surface oriented NNW-SSE. The side slopes (SSW and
82 NNE exposed) are gentle, the northern being only slightly steeper (14.1° vs 12.5° vs from the top down to
83 2900 m a.s.l.; Fig. 2, solid line). Despite their lithological homogeneity and their low porosity (< 5%, Berra,
84 personal communication), the two boreholes differ because in the PACE borehole two fractures filled by ice
85 were encountered at 42 and 90 m depth (Guglielmin et al., 2001) but no evidence of ice was observed
86 during the SSB drilling. Using PACE temperature profile and typical thermal conductivity and heat flow
87 values cited in literature (4.0 Wm⁻¹K⁻¹, Clauser and Huenges, 1995; 85 mWm⁻², Cermak et al., 1992),
88 permafrost thickness in the SSSB borehole was estimated to be around 220 m.

89

90 **3 METHODS**

91 **3.1 Field data**

92 The SSB borehole was drilled in early July, 2010, using refrigerated compressed-air-flush drilling technology.
93 The stratigraphy was obtained by analyses of the cuttings (sampled every 10 m) and, for the first 100 m,
94 through analysis of TV logging. Since September 2010, the thermal regime of the SSB borehole was
95 monitored with thermometers placed according to the PACE protocol (Harris et al., 2001). The accuracy of
96 the thermometers is 0.1°C and the resolution is 0.01°C. The thermistors recorded the daily ground
97 temperature (minimum, maximum and average) at 20, 25, 35, 40, 60, 85, 105, 125, 145, 165, 205, 215 and 235
98 m of depth. Since 1998, the main climatic parameters at the site (air temperature, snow cover, incoming
99 radiation) have been monitored. Below the 20m depth, no significant seasonal variations in temperature
100 are recorded.

101 **3.2 Laboratory data**

102 The thermal properties of the three main facies observed in the stratigraphy were measured in the
103 laboratory at three different temperatures (0°C, -1°C; -3°C). Thermal diffusivity and specific heat were
104 measured by NETZSCH Gerätebau GmbH (Selb, Germany) using a NETZSCH model 457 MicroFlash™ laser
105 flash diffusivity apparatus. Thermal diffusivity measurements were conducted in a dynamic helium
106 atmosphere at a flow rate of c. 100 ml/min between -3 °C and 0 °C. Specific heat capacity was measured
107 using the ratio method of ASTM-E 1461 (ASTM, 2003) with an accuracy of more than 5%. Density of the
108 rock at room temperature was determined using the buoyancy flotation method with an accuracy better
109 than 5%. Thermal conductivity was calculated following Carslaw and Jaeger (1959):

$$110 \quad \lambda = \rho \rho_p * c_p * \kappa$$

111 where λ is the thermal conductivity (W m⁻¹ K⁻¹), ρ_p is the bulk density (gcm⁻³), c_p is the specific heat
112 capacity (Jg⁻¹ K⁻¹), and κ is the thermal diffusivity (m² s⁻¹).

113 **3.3 Theory**

114 The temperature anomaly in the borehole at time t at depth z is modeled by the solution of the heat
115 equation

$$\frac{\partial A}{\partial t} - \frac{\partial}{\partial z} \left(\kappa \frac{\partial A}{\partial z} \right) = 0 \quad (1)$$

116 for the domain $(t, z) \in (-t_{max}, 0) \times (0, z_{max})$. Note that equation (1) can be derived from the classical
 117 formulation of Carslaw and Jaeger (1959) under the hypothesis that the density and the specific heat
 118 capacity are constant with respect to the depth z (see also Liu and Zhang, 2014), which is a good
 119 approximation for the SSB (see Section 4.1 and appendix). Further, we have indicated with t_{max} the earliest
 120 time for which we will reconstruct the GST and with z_{max} the depth of the borehole. Equation (1) can be
 121 solved to compute the temperature anomaly at any given past time t and depth z from the boundary values
 122 $A(t; 0)$ which represent the GST history. If the GST data $A(t, 0)$ are piece-wise constant, the solution of the
 123 direct problem for equation (1) can be found explicitly (see Carslaw and Jaeger, 1959). In our case, we need
 124 to solve the inverse problem of finding the GST from the borehole data, which provide the anomaly
 125 measured at present ($t=0$) or past times ($t>0$) at some depth z in the borehole.

126 In order to exploit the abovementioned explicit solution, it is customary to approximate the GST with a
 127 piece-wise constant function (see Figure 3)

$$GST(t) = \begin{cases} \tau_k, & t \in [-t_k, -t_{k-1}] \\ \tau_\infty, & t \leftarrow t_N \end{cases} \quad (2)$$

128 where t_k , for $k = 1, \dots, N$, is the sequence of times in the past where we want to compute the value of the
 129 GST, and the τ_k 's are the unknown values to be computed. The diffusive nature of the heat equation has
 130 the effect that fine details of GST signals are averaged away as time progresses. Therefore, in the field data,
 131 one can find signals coming only from long wavelength GST variations occurred in the distant past,
 132 whereas short wavelength signals are observable only if produced in the more recent history. In order to
 133 take into account long and short wavelengths variations of GST where each of them makes sense, contrary
 134 to the common use of choosing uniformly spaced time points, we choose

$$t_k = (1 + 0.2k)^2$$

135 so that the reconstruction points are closer to each other in the recent past and more separated for distant
 136 ages. The choice of the parameter 0.2 is such that the reconstructed GST can contain signals of wavelength
 137 of at least 33 years from 1600 onwards, 23 years from 1800 onwards, 16 years from 1915 onwards, 9 years
 138 from 1985 onwards.

139 Once the sequence t_k is chosen, the relation between the borehole temperature at depth z_j predicted by
 140 the model and the unknown values τ_k of the GST anomaly is linear. When comparing the anomaly $A(z, t)$
 141 described by the above equation with the measured data in the borehole, one has to take into account that
 142 measured data represent the superposition of the anomaly with a background signal (linearly increasing
 143 with depth) coming from the heat flow and past climatic changes since the Last Glacial Maximum as found
 144 for deeper boreholes by Safanda and Rajver (2001) or by Rath et al., (2012). This linear trend can be
 145 identified by linearly fitting the data from the deepest part of the borehole (below 60m in our case).
 146 Following (3), imposing that the borehole temperatures measured T_j years ago at depth z_j leads to a linear
 147 system

$$L\vec{\tau} = \vec{m}, \quad (4)$$

148 where the column vector $\vec{\tau} = [\tau_1, \tau_2, \dots, \tau_N, \tau_\infty]$ collects the unknown GST values, \vec{m} is the column vector
 149 of detrended measured data and L is a matrix with $M \times (J + 1)$ entries (see the appendix). Each row in L (and
 150 entry in the vector m), corresponds to a measured temperature in the well at present or at some time in

151 the past. In this fashion, the GST reconstruction can be based not only on a single temperature profile but
 152 also on the variation of the temperature profile between the present and some years ago. To the best of
 153 our knowledge, this possibility, which enhances the robustness of the reconstruction, has never been
 154 exploited before in the literature. Given the detrended measures \vec{m} , we must compute the vector $\vec{\tau}$ solving
 155 the linear system (4). However it is well known that the inverse problem for the heat equation (1) is severely
 156 ill-posed and thus solving directly the linear system (4) would lead to a computed GST that would be highly
 157 oscillating and very far from the true physical values for $\vec{\tau}$. It is then necessary to introduce a regularization
 158 process by modifying the original problem (4), in order to obtain an approximation that is well posed and
 159 less sensitive to errors in the right-hand-side of (4). Classical regularization techniques include the
 160 truncated singular value decomposition (TSVD) and the Tikhonov regularization in standard form (Hansen,
 161 1998), applied in Beltrami and Boulron, (2004) and Liu and Zhang, (2014), respectively. In this paper, we
 162 propose the use of the generalized Tikhonov regularization, where the damping term is measured by a
 163 proper seminorm. In practice, instead of dealing with the linear system (4), we solve the minimization
 164 problem

$$\min_{\vec{\tau}} \|L\vec{\tau} - \vec{m}\| + \alpha \|R\vec{\tau}\| \quad (5)$$

165 where $\alpha > 0$ is the regularization parameter and R is the regularization matrix. The use of a regularization
 166 matrix R for this application is a novelty although several other regularization smoothing parameters were
 167 already used (i.e. Shen et al., 1992; Rath and Mottaghy, 2007) If R is simply the identity matrix, then the
 168 problem (5) reduces to the standard Tikhonov method used in Liu and Zhang, (2014). When α is large the
 169 restored GST is very smooth but the differences between the measured data and the temperatures in the
 170 well that would be computed by (4) from the recovered GST are large. On the contrary, when α is too small
 171 the data fitting is good but the GST becomes highly oscillating due to the ill-posedness. A good tradeoff is
 172 not trivial and several strategies can be explored for estimating an optimal value of α : as an example, the
 173 generalized cross validation (Golub et al., 1979) often provides good results.

174 A common choice for R is a finite difference discretization of a differential operator (Hansen, 1998]. In this
 175 paper, we consider a standard discretization of the Laplacian so that the constant and linear components of
 176 the solution are not damped in the Tikhonov regularization, (5) while we have a penalization of high
 177 oscillations. The details of the chosen regularization and of the GST inversion employed are described in the
 178 appendix.

179 3.4 Validation on synthetic data

180 In order to validate our GST inversion method we have generated a synthetic data set as follows. An ideal
 181 GST was chosen (dashed curve in Fig. 4) and equation (1) was solved by a finite difference method with a
 182 spatial grid spacing of 1 m. Homogeneous Neumann boundary conditions were imposed at the well bottom
 183 and the ideal GST as Dirichlet data at $z=0$, thus obtaining synthetic data for the measurements of
 184 temperature in the well. The computed temperatures were saved for the depth at which the real
 185 thermometers in SBB are located (see Section 3.1), for the present time, as well as for 1, 2 and 3 years
 186 before present. We then used the generated data as input to the inversion algorithm described in the
 187 previous section and compared the reconstructed GST with the ideal one used to generate the synthetic
 188 data.

189 In the first experiment we fed our inversion algorithms only with the synthetic data for the present time.
 190 The value of alpha that best fits the exact GST is $\alpha=0.15$, but in Figure 4 one can see that also varying
 191 this value by 33% the reconstructed GST does not vary significantly.

192 Next we fed the inversion algorithm also with the synthetic data for the past years. First, the inversion is
193 expected to be more accurate since the algorithm can average not only on the temperature at a given
194 depth but also on the variation of the temperature in the last years at that depth. Moreover, the algorithm
195 should also be more robust, since it relies on a larger data set. Both these effects can be appreciated in Fig.
196 5, where it can be seen that the inversion in the last 50 years is more accurate than the inversion of Fig. 4
197 and that a wider variation in the value of alpha is possible without affecting very much the quality of the
198 reconstruction.

199

200 **4 RESULTS**

201 **4.1 Permafrost temperature, thermal properties and GST reconstruction**

202 The SSB stratigraphy is characterized by four different facies of dolostone (Figure 6): a massive dolostone
203 (from grey to pinky grey) comprises more than 90% of the profile; three other facies (white dolostone,
204 black stratified limestone, brownish dolostone) are thin intercalations (maximum 3.5 meters of thickness
205 and located mainly in the first 42 m). In particular facies d, was not analysed for thermal analyses because is
206 very limited and it does not have any lateral continuity.

207 The mean annual thermal profiles of the last three years (2013-14-15) show a negative gradient between
208 20 m (a depth corresponding approximately to the depth of zero annual amplitude, ZAA) and 60 m that
209 does not vary (-0.8°C/100 m in all the three years). At greater depth, the gradient is positive with slightly
210 different slopes between 60-105; 105-125; 125-205; 205-215 and 215-235 (Figure 7 and Table 1).

211 Table 2 shows the thermal properties of the three main stratigraphic facies encountered in the borehole.
212 Facies a and c show similar density and thermal properties while facies b has higher density and higher
213 conductivity. All facies have heat capacity values that increase with a decrease of temperature. In facies a,
214 this behavior occurs also for thermal conductivity and diffusivity values. In contrast, facies b and c show a
215 reversed bell shape behavior, with the minimum value recorded at -1°C and an absolute maximum at -3°C.
216 Therefore, from a thermal point of view, only facies b is different. Moreover, at depths below the level of
217 zero annual amplitude, this facies occurs only at depths of 34.5m and 90 m with a negligible thickness (2
218 and 1 m respectively) and at 142.5 m and 205 m where it reaches 3-3.5 m in thickness. Clearly, the thermal
219 influence of this facies is negligible, indeed, the gradient between 60 and 235 m is approximately the same
220 as that between 60 and 105 m and between 125 and 205 m. The effects of the different thermal
221 diffusivities measured in the different facies of the SSB borehole are also illustrated in Figure 8 where is
222 possible to notice that the difference of temperature *a posteriori* between a model with a constant
223 diffusivity equal to the average value of the facies a between 0°C and -1°C (red dots) and the model with
224 the different diffusivities for each different facies layer (blue dots) is absolutely negligible (< 0.02°C) in all
225 the depths with the exception of the uppermost (20 m) where the difference is higher but still very low
226 (0.06°C).

227 According to the model proposed in the Methods, we found the best fitting with the thermal profiles
228 (Figure 7) using an heat flow of 70 mWm⁻² (Della Vedova et al., 1995), a thermal diffusivity value equal to
229 the mean between the value obtained for 0°C and -1°C for facies a, which is the more widespread in the
230 borehole and an alpha value of 0.95 as shown in figure 9.

231 The linear system (4) was assembled including the detrended data measured at SSB in 2015 ($T_j = 0$, in
232 2014 ($T_j = 1$ and 2013 ($T_j = 2$, at the 13 depths listed in Section 3.1, resulting in 39 equations. The
233 anomalies of the GST reconstruction obtained with respect to the reference period between 1880 and 1960
234 has been computed using the value of $\alpha = 0.95$ for the regularization parameter (Figure 10).

235

236 **5 DISCUSSION**

237 **5.2.1 GST and current air temperatures**

238 In cryotic environments, snow cover can influence GST variability both in space and in time (e.g. Zhang,
239 2005; Schmidt et al., 2009; Morse et al., 2012; Rodder and Kneisel, 2012; Schmid et al., 2012; Guglielmin et
240 al., 2014). This is especially the case for alpine areas where topography influences both the re-distribution
241 of the snow by wind-drift and actual snow cover evolution (e.g. melting date and duration). Nevertheless,
242 GST and air temperature are well correlated ($R^2 = 0.8027$) and present a very similar pattern over the last
243 15 years with only a slight warming (Figure 11). This relatively slight effect of snow at this site is probably
244 due to the high wind velocities during winter that, on average, prevent buildup of a thick snowpack. Figure
245 12 illustrates the temporal variability of snow cover on the GST. In general, the highest ($>\pm 5^\circ\text{C}$) differences
246 between mean daily GST and mean daily air temperature occur when there are large drops of air
247 temperature during the winter. Sometimes, large differences occur also when there are large drops of air
248 temperature during the summer where there is little or no snow cover, because of high solar radiation that
249 heats the ground surface. Correlation is even better between monthly mean air temperature, mean annual
250 air temperature (MAAT) and mean annual ground surface temperature (MAGST) ($R^2 = 0.8712$ for this
251 latter). This agrees with the results of Zhang and Stamnes, (1998) who found that, in a flat area in northern
252 Alaska, changes in seasonal snow cover had a smaller effect than MAAT on the ground thermal regime.

253 **5.2.2. GST Fluctuations between 1950 and today**

254 Our reconstruction after the cold GST anomaly, between 1906 and 1941 AD, shows a slightly positive peak
255 (ca. 0.1°C) in 1930 and afterwards a very unstable period with a first sharp decrease of temperature until
256 1989 (between -0.2 and -0.6°C) and a second even sharper increase, reaching in 2011 the uppermost GST
257 anomaly value of the last 500 years (around 1°C).

258 On a regional scale, the Stelvio data can be compared with the MAAT obtained for the Alps by Christiansen
259 and Ljungqvist, (2011) (Figure 10) and Trachsel et al., (2010). The maximum of the slight temperature
260 increase during the first half of the XX century in the Stelvio data (1930) falls exactly in the middle of the
261 relative warming period between 1925 and 1935 in the Alps found by Trachsel et al., (2010) and is in good
262 agreement with the date (1928) indicated by Christiansen and Ljungqvist, (2011). Later, the sharp GST
263 anomaly decrease was delayed in the Stelvio data (1989) with respect to 1950-1965 period found by
264 Trachsel et al., (2010) and 1965-1975 period found by Christiansen and Ljungqvist, (2011). Finally, the most
265 recent increase of temperature culminated in the Alps in 1994 (Christiansen and Ljungqvist, 2011) while in
266 the Stelvio data at 2011.

267 **5.2.3 The Little Ice Age (LIA)**

268 The Stelvio reconstruction shows a long period of negative anomaly between 1560 and 1860 AD with the
269 colder conditions (< -2 *S.D.) between 1683 and 1784 AD with a peak of -1.5°C around 1730 AD. This period

270 of negative anomaly falls within this well-known cooling period (LIA). It is recognized in several kinds of
271 proxy data although there are differences both in magnitude and in timing across the world. According to
272 Neukom et al., (2014), synchronous cold temperature anomalies occurred at decadal scale in both
273 hemispheres between 1594 and 1677 AD. They also found two phases of extreme cold temperature in the
274 Northern Hemisphere with the first between 1570 and 1720 AD and the second between 1810 and 1855.
275 Syntheses of the LIA in the European Alps have been presented by Trachsel et al., (2012) and Christiansen
276 and Ljungqvist, (2011). Considering the common colder periods in these two Alpine syntheses, the LIA has
277 three main negative peaks at 1570-1600; 1685-1700 and 1790-1820 AD.

278 The LIA period has been also characterized by a widespread worldwide glacier advance, although the
279 comparison between glacial evidences and temperature fluctuations are problematic because glaciers
280 respond with different time scales (mainly depending on their size) and reflect also the precipitation
281 regime, which is even more variable in space and time. According to Holzhauser et al., (2005), the LIA
282 advance of the main Swiss Glaciers has three peaks around respectively 1350, 1640 and 1820-50 AD with
283 the two later phases almost synchronous also in the Eastern Alps (Nicolussi and Patzelt, 2000).

284 Close to the location of the Stelvio borehole, the maximum LIA advance was diachronous. Nearby glaciers
285 show a maximum LIA advance in 1580 AD (Trafoi Valley glacier; Cardassi, 1995), around 1770 AD (Solda
286 Glacier; Arzuffi and Pelfini, 2001) and in 1600 AD (La Mare Glacier; Carturan et al., 2014).

287 The borehole area was presumably overcapped by the Vedretta Piana Glacier until 1868. Due to the
288 geomorphological position (on a watershed divide) the possible glacier should have been very thin and
289 possibly cold based, as already stressed by Guglielmin et al., (2001). On the other hand, considering figure
290 10, the glacier should have been present in the borehole area with a buffering effect only between 1711
291 and 1834 AD, with a peak at 1760, when the difference between the GST anomaly and the MAAT anomaly
292 was maximum. This peak is pretty similar to the peak of the LIA in the Solda Glacier (1770 AD) but not to
293 the peak in the Trafoi glacier (1580 AD); this could be related to Vedretta Piana having a more similar
294 glacier size and aspect (NE-N) to the Solda Glacier than to the Trafoi Glacier, although this latter is the
295 closest to the Vedretta Piana.

296 **5.2.4 Other permafrost borehole temperature reconstructions**

297 Several deep Alaskan boreholes have been used to demonstrate the XX century warming (e.g. Lachenbruch
298 and Marshall, 1986; Lachenbruch et al., 1988) but only a few studies in Europe illustrate GST
299 reconstructions that span a time period greater than 100-150 years (e.g. Isaksen et al., 2001, Guglielmin,
300 2004). In North America, only Chouinard et al., (2013) shows GST pattern of the last 300 years in the
301 context of the permafrost of Northern Quebec. There, after the LIA (1500-1800 AD), it was found an almost
302 constant and marked warming of ca 1.4 °C until 1940, followed by a cooling episode (≈ 0.4 °C) which lasted
303 40–50 yr, and finally a sharp ≈ 1.7 °C warming over the past 15 yr.

304 There is a some similarity between the Stelvio reconstruction and the pattern of Canadian permafrost GST
305 reported by Chouinard et al., (2013) after the LIA. Indeed, also in our site there was an almost simultaneous
306 but greater cooling (0.9°C) in the period between 1941 and 1989, followed by a sharp warming of ca 1.7°C.
307 On the other hand, GST reconstructions can be obtained with different models and it is interesting to
308 compare our data with, for example, the PMIP3/CMIP5 simulations that include the effect of aerosol
309 forcing by Garcia-Garcia et al., (2016): there, in the last 500 years, the GST shows a cold anomaly (LIA)
310 between 1582 and 1840, with the most negative peaks between 1798 and 1840, slightly delayed with
311 respect to our data.

312

313 **5 CONCLUSIONS**

314 The general climatic pattern of the last 500 years recorded by this mountain permafrost borehole is similar
315 to the majority of other studies in the European Alps and Central Europe. The main difference concerns
316 post LIA events. In fact, the different multidisciplinary proxies considered (see Figure 13) do not indicate
317 cooling between 1940 and 1989, with the exceptions of the shorter and less severe cooling found for the
318 Alps. It is also relevant to stress that the rapid and abrupt GST warming (more than 0.8°C per decade)
319 recorded between 1990 and 2011 in the Stelvio borehole data is similar to the warming recorded in
320 permafrost in northern Quebec. This warming trend is of the same magnitude as the increase of MAAT
321 between 1990 and 2000 in Central Europe (Dobrovlny et al., (2010), and is approximately double that found
322 for the MAAT in the Alps and for Europe as a the whole (Luterbacher et al., 2004).

323 The Stelvio borehole ground surface temperature reconstruction also allows one to estimate changes in the
324 Vedretta Piana glacier. This glacier presumably buried the site of the Stelvio borehole with an ice thickness
325 sufficient to exert a significant buffering effect upon the ground thermal regime between 1711 and 1834
326 AD. This was a time when the difference between the Stelvio GST anomaly and the MAAT anomaly was
327 greatest.

328

329 **6 REFERENCES**

- 330 Arzuffi, L. and Pelfini, M., I testimoni dei cambiamenti climatici, *Neve e Valanghe*, 43, 44–53, 2001.
- 331 Auer, I., Böhm, R., Jurkovic, A., Lipa, W., Orlik, A., Potzmann, R., Schöner, W., Ungersböck, M., Matulla, C.,
332 Briffa, K., Jones, P., Efthymiadis, D., Brunetti, M., Nanni, T., Maugeri, M., Mercalli, L., Mestre, O., Moisselin,
333 J.M., Begert, M., Müller-Westmeier, G., Kveton, V., Bochnicek, O., Stastny, P., Lapin, M., Szalai, S.,
334 Szentimrey, T., Cegnar, T., Dolinar, M., Gajic-Capka, M., Zaninovic, K., Majstorovic, Z and Nieplova, E.
335 HISTALP-historical instrumental climatological surface time series of the Greater Alpine Region, *Int. J.*
336 *Climatol.*, 27, 17–46, 2007.
- 337 Barbante, C., et al. Historical record of European emissions of trace elements to the atmosphere since the
338 1650s from alpine snow/ice cores drilled near Monte Rosa, *Environ. Sci. Technol.* 38,15, 4085–4090, 2004.
- 339 Beltrami, H. and Bourlon, E. Ground warming patterns in the northern hemisphere during the last five
340 centuries, *Earth Planet. Sc. Lett.*, 227, 169–177, 2004.
- 341 Bodri, L. and Cermak, V., Climate changes of the last millennium inferred from borehole temperatures:
342 results from the Czech Republic Part I, *Global and Planetary Change*, 98, 111-125,1995.
- 343 Böhm, R., Auer, I., Brunetti, M., Maugeri, M., Nanni, T.and Schöner W. Regional temperature variability in
344 the European Alps: 1760-1998 from homogenized instrumental time series, *Int. J. Climatol.*, 21, 1779–1801,
345 2001.
- 346 Büntgen, U., Frank, D. C., Nievergelt, D. and Esper, J., Summer temperature variations in the European Alps,
347 A.D. 755–2004, *J. Climate*, 19, 5606–5623.,2006.

- 348 Cardassi, S.P. Geologia del Quaternario e geomorfologia della Valle di Trafoi. Master's Thesis, University of
349 Milan, 1995.
- 350 Carslaw, H.S. and Jaeger, J.C. Conduction of Heat in Solids. Oxford Univ. Press, New York. 510 pp. 1959.
- 351 Carturan, L., Baroni, C., Carton, A., Cazorzi, F., Dalla Fontana, G., Delpero, C., Salvatore, M.C., Seppi, R. and
352 Zanoner, T., Reconstructing fluctuations of La Mare Glacier (Eastern Italian Alps) in the Late Holocene: new
353 evidence for a Little Ice Age maximum around 1600 ad., *Geografiska Annaler: Series A, Physical Geography*,
354 96, 287–306, 2014.
- 355 Cermak, V., Balling, N., Della Vedova, B., Lucazeau, F., Pasquale, V., Pellis, G., Schulz, R. and Verdoya, M.,
356 Heat-flow data (Italy). In: Blundell, D., Freeman, R., Mueller, St. (Eds.), *A Continent Revealed: The European*
357 *Geotraverse Database*. Cambridge Univ. Press, Cambridge, pp. 49– 57, 1992.
- 358 Chouinard, C., Fortier, R. and Mareschal J.C. Recent climate variations in the subarctic inferred from three
359 borehole temperature profiles in northern Quebec, Canada, *Earth and Planetary Science Letters*, 263, 355–
360 369, 2007.
- 361 Christiansen, B. and Ljungqvist, F. C. Reconstruction of the extratropical NH mean temperature over the last
362 millennium with a method that preserves low-frequency variability, *J. Climate*, 24, 6013-6034, 2011.
- 363 Clauser C, and Huenges E. Thermal conductivity of rocks and minerals. In *Rock Physics and Phase Relations.*
364 *A Handbook of Physical Constants*, Ahrens TJ (ed). AGU Reference Shelf 3. American Geophysical Union:
365 Washington; 105–126, 1995.
- 366 Cook, B.I., Bonan, G.B., Levis, S. and Epstein, H.E., The thermoinsulation effect of snow cover within a
367 climate model, *Clim. Dyn*, 31, 107–124, 2008.
- 368 Corona, C., Guiot, J., Edouard, J.L., Chalié, F., Büntgen, U., Nola, P. and Urbinati, C., Millennium-long
369 summer temperature variations in the European Alps as reconstructed from tree rings. *Climate of the Past*,
370 6, 379-400, 2010.
- 371 Della Vedova, B., Lucazeau, F., Pasquale, V., Pellis, G. and Verdoya., M. Heat flow in the tectonic provinces
372 crossed by the southern segment of the European Geotraverse, *Tectonophysics*, 244 ,57-74, 1995
- 373 Dobrovolný, P., Moberg, A., Brázdil, R., Pfister, C., Glaser, R., Wilson, R., van Engelen, A., Limanówka, D.,
374 Kiss, A., Halíčková, M. Macková, J. Riemann, D. Luterbacher, J. and Böhm R., Monthly, seasonal and
375 annual temperature reconstructions for Central Europe derived from documentary evidence and
376 instrumental records since AD 1500, *Climatic Change*, 101, 69–107, 2010.
- 377 García-García, A., Cuesta-Valero, F. J., Beltrami, H. and Smerdon, J. E. Simulation of air and ground
378 temperatures in PMIP3/CMIP5 last millennium simulations: implications for climate reconstructions from
379 borehole temperature profiles, *Environmental Research Letters*, 11, 044022, 2016
- 380 Golub, G. H., Heath M. and Wahba G., Generalized Cross-Validation as a Method for Choosing a Good Ridge
381 Parameter, *Technometrics*, 21 ,2, 215-223, 1979.
- 382 Gruber, S., King, L., Kohl, T., Herz, T., Haeberli, W. and Hoelzle, M., Interpretation of geothermal profiles
383 perturbed by topography: the Alpine permafrost boreholes at Stockhorn Plateau, Switzerland, *Permafrost*
384 *and Periglacial Processes*, 15, 349–357, 2004.

- 385 Guglielmin, M., Observations on permafrost ground thermal regimes from Antarctica and the Italian Alps,
386 and their relevance to global climate change, *Global and Planetary Change*, 40, 159–167, 2004.
- 387 Guglielmin, M., Cannone, N. and Dramis, F., Permafrost-glacial evolution during the Holocene in the Italian
388 Central Alps, *Permafrost Periglacial Processes*, 12, 111–124, 2001
- 389 Guglielmin, M., Worland, M.R., Baio, F. and Convey, P., Permafrost and snow monitoring at Rothera Point
390 (Adelaide Island, Maritime Antarctica): Implications for rock weathering in cryotic conditions,
391 *Geomorphology*, 225, 47–56, 2014.
- 392 Hansen, P., Rank-Deficient and Discrete Ill-Posed Problems, Society for Industrial and Applied Mathematics,
393 1998.
- 394 Harris, C., Haeberli, W., Vonder Muhll, D. and King, L., Permafrost monitoring in the high mountains of
395 Europe: the PACE Project in its global context, *Permafrost and Periglacial Processes*, 12, 3 – 11, 2001.
- 396 Harris, C., Vonder Mühll, D., Isaksen, K., Haeberli, W., Sollid, J.I., King, L., Holmlund, P., Dramis, F.,
397 Guglielmin, M. and Palacios, D., Warming permafrost in European mountains, *Global and Planetary Change*,
398 39, 215-225, 2003.
- 399 Hilbich, C., Hauck, C., Hoelzle, M., Scherler, M., Schudel, L., Völksch, I., Vonder Mühll, D. and Mäusbacher,
400 R., Monitoring mountain permafrost evolution using electrical resistivity tomography: a 7-year study of
401 seasonal, annual, and long-term variations at Schilthorn, Swiss Alps, *J. Geophys. Res.*, 113, F01S90. 2008.
- 402 Holzhauser, H., Magny, M. and Zumbühl, H.J., Glacier and lake-level variations in west-central Europe over
403 the last 3500 years, *The Holocene*, 15, 6, 789–801, 2005.
- 404 Huang, S., Pollack, H. N. and Shen, P. Y., Temperature trends over the last five centuries reconstructed from
405 borehole temperatures, *Nature*, 403, 756–758, 2000.
- 406 IPCC. Summary for policymakers, In *Climate Change 2013: The Physical Science Basis. Contribution of*
407 *Working Group I to the Fifth Assessment Report of the Intergovernmental Panel on Climate Change*,
408 Stocker, T.F., Qin, D., Plattner, G.K., Tignor, M.S.K., Allen, J., Boschung, A., Nauels, Y., Xia, Y., Bex, V.,
409 Midgley, P.M., (eds). Cambridge University Press: Cambridge, UK and New York, NY, 2013.
- 410 Isaksen, K., Vonder Muhll, D., Gubler, H., Kohl, T. and Sollid, J.L., Ground surface-temperature
411 reconstruction based on data from a deep borehole in permafrost at Janssonhaugen, Svalbard, *Annals of*
412 *Glaciology*, 31, 287– 294. 2001.
- 413 Lachenbruch, A.H. and Marshall, B.V., Changing climate: geothermal evidence from permafrost in the
414 Alaskan Arctic, *Science* 234, 689– 696, 1986.
- 415 Lachenbruch, A.H., Cladouhos, T.T. and Saltus, R.W., Permafrost temperature and the changing climate.
416 “Permafrost”, 5th International Permafrost Conference Proceedings, vol. 3. Tapir Publishers, Trondheim,
417 Norway, pp. 9–17, 1988.
- 418 Larocque-Tobler, I., Grosjean, M., Heiri, O., Trachsel, M., and Kamenik, C. Thousand years of climate change
419 reconstructed from chironomid subfossils preserved in varved lake Silvaplana, Engadine, Switzerland,
420 *Quaternary Science Reviews*, 29, 1940–1949, 2010.

- 421 Lewis, T. J. and K. Wang, Influence of terrain on bedrock temperatures, *Palaeogeogr. Palaeoclimatol.*
 422 *Palaeoecol.* 98, 87–100, 1992
- 423 Ling, F. and Zhang, T.J., Sensitivity of ground thermal regime and surface energy fluxes to tundra snow
 424 density in northern Alaska, *Cold Reg. Sci. Technol.*, 44, 121–130, 2006.
- 425 Liu J. and Zhang T., Fundamental solution method for reconstructing past climate change from borehole
 426 temperature gradients, *Cold Regions Science and Technology*, 102, 32-40, 2014.
- 427 Luterbacher, J., Dietrich, D., Xoplaki, E., Grosjean, M., and Wanner, H., European seasonal and annual
 428 temperature variability, trends, and extremes since 1500, *Science*, 303, 1499–1503, 2004.
- 429 Morse, P.D., Burn, C.R. and Kokelj, S.V., Influence of snow on near-surface ground temperatures in upland
 430 and alluvial environments of the outer Mackenzie Delta, N.W.T. *Can. J. Earth Sci.*, 49, 895–913, 2012.
- 431 Mottaghy, D. and Rath, V., Latent heat effects in subsurface heat transport modelling and their impact on
 432 palaeotemperature reconstructions, *Geophysical Journal International*, 164, 236-245, 2006
- 433 Neukom, R., Gergis, J., Karoly, D.J., et al. Inter-hemispheric temperature variability over the past
 434 millennium, *Nature Climate Change*, 4, 362–367, 2014.
- 435 Nicolussi, K. and Patzelt, G., Discovery of early Holocene wood and peat on the forefield of the Pasterze
 436 Glacier, Eastern Alps, Austria, *The Holocene*, 10, 191–199, 2000.
- 437 Rath, V. and Mottaghy, D., Smooth inversion for ground surface temperature histories: estimating the
 438 optimum regularization parameter by generalised cross-validation, *Geophysical Journal International*, 171
 439 (3), 1440-1448, 2007
- 440 Rath, V., Gonzalez-Rouco, J. F. and Goosse, H., Impact of postglacial warming on borehole reconstructions
 441 of last millennium temperatures, *Climate of the Past*, 8, 1059-1066, 2012.
- 442 Rodder, T. and Kneisel, C., Influence of snow cover and grain size on the ground thermal regime in the
 443 discontinuous permafrost zone, Swiss Alps. *Geomorphology*, 175-176, 176–189, 2012.
- 444 Safanda, J. and Rajver, D., Signature of the last ice age in the present subsurface temperatures in the Czech
 445 Republic and Slovenia, *Global and Planetary Change*, 29, 241-257, 2001.
- 446 Schmid, M.O., Gubler, S., Fiddes, J. and Gruber, S., Inferring snowpack ripening and melt-out from
 447 distributed measurements of near-surface ground temperatures, *The Cryosphere*, 6, 1127–1139, 2012.
- 448 Schmidt, S., Weber, B. and Winiger M., Analyses of seasonal snow disappearance in an alpine valley from
 449 micro- to meso-scale (Loetschental, Switzerland), *Hydrol. Process.*, 23, 1041–1051, 2009.
- 450 Serra-Capizzano, S., A note on the antireflective boundary conditions and fast deblurring models, *SIAM*
 451 *Journal on Scientific Computing*, 25-4, 1307–1325, 2004.
- 452 Shen, P. Y., Wang, K. H. and Beltrami Mareschal, J.C., A comparative study of inverse methods for
 453 estimating climatic history from borehole temperature data, *Palaeogeogr. Palaeoclimatol. Palaeoecol.* (GPC
 454 section), 98, 113-127, 1992.
- 455 Trachsel, M., Grosjean, M., Larocque-Tobler, I., Schwikowski, M., Blass, A., Sturm, M., Quantitative summer
 456 temperature reconstruction derived from a combined biogenic Si and chironomid record from varved

457 sediments of Lake Silvaplana (south-eastern Swiss Alps) back to AD 1177. *Quaternary Science Reviews*, 29,
458 2719-2730, 2010.

459 Trachsel, M., Kamenik, C., Grosjean, M., McCarroll, D., Moberg, A., Brázdil, R., Büntgen, U., Dobrovlný,
460 P., Esper, J., Frank, D. C., Friedrich, M., Glaser, R., Larocque-Tobler, I., Nicolussi, K. and Riemann D.,
461 Multi-archive summer temperature reconstruction for the European Alps, AD 1053–1996, *Quaternary*
462 *Science Reviews*, 46, 66-79, 2012.

463 Zhang, T., Influence of the seasonal snow cover on the ground thermal regime: An overview, *Rev. Geophys.*,
464 43, RG4002, 2005.

465 Zhang, T. and Stamnes K., Impact of climatic factors on the active layer and permafrost at Barrow, Alaska,
466 *Permafrost Periglacial Processes*, 9, 229–246, 1998.

467

468 **7 ACKNOWLEDGEMENTS**

469 The SSB borehole was drilled and equipped thanks to the Project “Share Stelvio” managed by EvK2-CNR and
470 funded by Regione Lombardia. The research was also funded through the PRIN 2008 project “Permafrost e
471 piccoli ghiacciai alpini come elementi chiave della gestione delle risorse idriche in relazione al Cambiamento
472 Climatico” led by Prof. C. Smiraglia. Special thanks to the Stelvio National Park, SIFAS and Umberto
473 Capitani for the permissions and the logistical support. We want also to thank you very much Prof. Hugh M.
474 French for the revision and the English editing of the manuscript.

475

476 **Figure and Table Captions**

477 Figure 1. Study area: (a) Location of the study area with the surrounding glaciers and the reconstructed
478 glaciers limits of the area (VPG = Vedretta Piana Glacier; TFG = Trafoi Glacier; SG = Solda Glacier; LMG = La
479 Mare Glacier; PACE = Pace Borehole; SSB = Share Stelvio Borehole; (b) View of the drilling equipment during
480 the realization of the SSB borehole in summer 2009.

481 Figure 2. Topography of the SSB site: a) Digital Elevation Model (5 m resolution) of the SSB site and b) SSW-
482 NNE (solid line) and N-S (dashed line) transects through the Stelvio summit. Horizontal and vertical scales
483 as well as thermistor chain position and depths are plotted to the same scale.

484 Figure 3. Example of a GST history parametrized by equation (2).

485 Figure 4. Synthetic data for the present time. It is remarkable that also varying the alpha value by 33% the
486 reconstructed GST does not vary significantly. Legend: 0.1 = blue line; 0.15 = green line; 0.2 = orange line.

487 Figure 5. Synthetic data for three past years (2013, 2014 and 2015). It can be seen that the inversion in the
488 last 50 years is more accurate than the inversion of Fig 4. Legend: 0.15 = green line; 0.2 = orange line; 0.25 =
489 red line.

490 Figure 6. Share Stelvio Borehole (SSB) Stratigraphy. Legend: (A) facies a (massive dolostone from grey to
491 pinky grey); (B) facies b (white dolostone); (C) facies c (black stratified limestone); (D) facies d (light brown
492 dolostone).

493 Figure 7. SSB mean annual ground temperature profiles on 2013, 2014 and 2015.

494 Figure 8 Effects of different thermal diffusivity used in the model. The temperature profiles *a posteriori* of
495 2015 obtained in the case of a constant thermal diffusivity value of the more widespread facies (a) (red
496 dots) and in the case of with a multilayers thermal diffusivities according the different facies according Fig.
497 6 (blue dots). The bars indicate the variations of the measured temperature in the same year.

498 Figure 9 Example of different GST history with different alpha with the extreme of heat flow values known
499 for the region. Legend: green lines are obtained with a heat flow of 70 mWm⁻² while red lines with 85
500 mWm⁻². The different symbols indicate different alpha value (0.95 = solid line; 1.1 = empty dots; 0.8 =
501 triangles).

502 Figure 10. Comparison between the anomaly of the mean annual GST reconstructed by SSB borehole (black
503 thick line), its uncertainty range (red shaded) and MAAT anomaly reconstructed for the European Alps by
504 Christiansen and Ljungqvist (2011) (grey line with dots; data available online at:
505 <https://www.ncdc.noaa.gov/paleo/study/12355>) both respect the same reference period (1880-1960).

506 Figure 11. Trend of monthly mean of GST (red line) and Air temperature (blue line) at SSB since 1998. The
507 red and blue dashes lines are respectively the linear regression of the GST and Air temperature.

508 Figure 12. Effect of the snow cover at SSB. The winter 2010/11 is representative of the average conditions
509 of the snow cover at SSB while the following season 2011/12 was the snowiest of the whole monitoring
510 period. The difference between the daily mean GST and air temperature (Δ GSTair; black line) shows the
511 greater values during the greater drop of the air temperature (green line) during the winter due to the
512 insulating effect of the snow cover (blue line) whereas the few episodes of high Δ GSTair in the summer are
513 may due to the solar radiation that warms up the ground surface.

514 Figure 13. Main climatic events enhanced by anomalies of MAAT through different proxy in all Europe: A,
515 (modified from Luterbacher et al., 2004); Central Europe: B, (rielaborated from Dobrovolný et al., 2010;
516 Alps: C, (modified from the same data of Figure 5, Christiansen and Ljungqvist, 2011) and SSB: D, (this
517 paper).

518 Figure 14. Comparison of predictions of the forward model for the same GST and different geometrical
519 setups. Legend: 1D = red dots; 2D flat terrain = blue line; 2D N-S green line; 2D SSW-NNE orange line; 3D
520 dashed black line. (See the Appendix for the details).

521 Table 1. Thermal gradients (°Cm⁻¹) on 2013; 2014 and 2015 in the different depth intervals of the profile
522 below the zero-annual amplitude that is approximately at 20 m of depth.

523 Table 2. Thermal properties of the three different facies occurred in SSB borehole measured in the
524 Laboratory at three different steps of temperature (0; -1 and -2°C).

525 Table 1

	20-60 m (°Cm ⁻¹)	60-105 m (°Cm ⁻¹)	105-125 m (°Cm ⁻¹)	125-205 m (°Cm ⁻¹)	205-215 m (°Cm ⁻¹)	215-235 m (°Cm ⁻¹)	60-235 m (°Cm ⁻¹)
2013	0.0088	-0.0072	-0.0048	-0.0075	-0.0128	-0.0058	-0.0072
2014			-0.0046	-0.0074	-0.0128	-0.0056	
2015	0.0086	-0.0077	-0.0045	-0.0073	-0.0128	-0.0055	-0.0072

526

527

528 Table 2

	Density (gcm ⁻³)	Diffusivity (10 ⁻⁶ m ² s ⁻¹)	Heat capacity (Jg ⁻¹ K ⁻¹)	Conductivity (Wm ⁻¹ K ⁻¹)
Facies a	2.7			
0°C		2.2	0.7	4.5
-1°C		2.1	0.8	4.4
-3°C		2.1	0.8	4.4
Facies b	2.8			
0°C		2.8	0.8	6.2
-1°C		2.8	0.8	6.2
-3°C		2.8	0.8	6.2
Facies c	2.7			
0°C		2.0	0.8	4.0
-1°C		1.9	0.8	3.9
-3°C		1.9	0.8	4.0

529

530 **Appendix 1: Details of the regularization and inversion technique**

531 The temperature anomaly in the borehole at time t at depth z is modeled by the solution of the heat
532 equation

$$\frac{\partial A}{\partial t} - \frac{\partial}{\partial z} \left(\kappa \frac{\partial A}{\partial z} \right) = 0(1)$$

533 for the domain $(t, z) \in (-t_{max}, 0) \times (0, z_{max})$. If the boundary data $A(t, 0)$ is piece-wise constant, then
534 the solution of the direct problem for equation (1) can be found explicitly (see Carslaw and Jaeger, 1959). In
535 fact, the anomaly observed in the borehole t years ago, originating from a GST that has been constant
536 except for an increase of δ °C between t_2 and t_1 years ago is:

$$A(t, z) = \delta \left[\operatorname{erfc} \left(\frac{z}{\sqrt{4\kappa(t_2 - t)}} \right) - \operatorname{erfc} \left(\frac{z}{\sqrt{4\kappa(t_1 - t)}} \right) \right]$$

537 The above formula of course makes sense only for $t < t_1$ and the value $t = 0$ corresponds to present time.
538 For the purpose of reconstructing the GST history, it is customary to approximate it with a piece-wise
539 constant function (see Figure 3)

$$GST(t) = \begin{cases} \tau_k, & t \in [-t_k, -t_{k-1}] \\ \tau_\infty, & t \leftarrow t_N \end{cases} (2)$$

540 where t_k , for $k = 1, \dots, N$, is the sequence of times in the past where we want to compute the value of the
541 GST, and the τ_k 's are the unknown values to be computed. The prediction of model (1) for the borehole
542 temperature t years ago, originating from the GST (2) is

$$A(z, t) = \tau_1 \varphi(z, t_1 - t) + \sum_{k=1}^N \tau_k [\varphi(z, t_{k+1} - t) - \varphi(z, t_k - t)] - \tau_\infty \varphi(z, t_N - t), (3)$$

543 where $\varphi(z, t) = \text{erfc}\left(\frac{z}{\sqrt{4\kappa t}}\right)$. Note that, once the sequence t_k is chosen, the relation between the borehole
 544 temperature at depth z_j predicted by the model and the unknown values τ_k of the GST anomaly is thus
 545 linear. The matrix L of the linear system (4) in the main text is thus

$$\begin{aligned} L_{j,1} &= \varphi(Z_j, t_1 - T_j) \\ L_{j,k} &= \varphi(Z_j, t_{k+1} - T_j) - \varphi(Z_j, t_k - T_j) \\ L_{j,N+1} &= \varphi(Z_j, t_N - T_j). \end{aligned}$$

546 We point out that each row of the matrix L can have a different value of T_j , so that the GST reconstruction
 547 can be based not only on a single temperature profile, but also on the variation of the temperature profile
 548 between the present and some years ago. Further, it is not needed that the reconstruction times t_k are
 549 equally spaced in the past.

550 Given the detrended measures \vec{m} , we must compute the vector $\vec{\tau}$ solving the linear system (4). Note that
 551 the inverse problem for the heat equation (1) is well-known to be severely ill-posed, the matrix L is strongly
 552 ill-conditioned and its singular values decay exponentially to zero, with related singular vectors largely
 553 intersecting the subspace of high frequencies (Serra-Capizzano, 2004). Therefore, since the right-hand side
 554 \vec{m} is affected by error measurements, solving directly the linear system (4) would lead to a computed GST
 555 that would be highly oscillating and very far from the true physical values for $\vec{\tau}$. It is then necessary to
 556 introduce a regularization process by modifying the original problem (4), in order to obtain an
 557 approximation that is well posed and less sensitive to errors in the right-hand-side of (4). The Tikhonov
 558 regularization usually provides better restorations than the truncated SVD, because it is characterized by a
 559 smooth transition in the filtering of the frequencies and the smoothness of the transition can be somehow
 560 chosen by manipulating the regularization parameter of the method (Hansen, 1998). In this paper, we thus
 561 propose the use of the generalized Tikhonov regularization, where the damping term is measured by a
 562 proper seminorm. In practice, instead of dealing with the linear system (4), we solve the minimization
 563 problem

$$\min_{\vec{\tau}} \|L\vec{\tau} - \vec{m}\| + \alpha \|R\vec{\tau}\| \quad (5)$$

564 where $\alpha > 0$ is the regularization parameter and R is the regularization matrix. The presence of the matrix
 565 R in (5) allows to impose some a-priori information on the true solution. Indeed, when minimizing (5), the
 566 components of the solution belonging to $\ker(R) = \{\vec{x} \text{ s.t. } R\vec{x} = \vec{0}\}$ are perfectly reconstructed. In fact, if a
 567 vector x belongs to $\ker(R)$ then $\|R\vec{x}\| = 0$ and hence the penalization term disappears in the minimization
 568 problem (5) and consequently the data are perfectly fitted. Note that in order to guarantee the uniqueness
 569 of the solution (5), the condition $\ker(L) \cap \ker(R) = \vec{0}$ has to hold.

570 In this paper, we use as regularizer a standard discretization of the Laplacian

571

$$R = \begin{pmatrix} & & & -1 & & & & \\ & & & & & & & \\ & & & & & & & \\ -1 & & & -1 & 2 & -1 & & \ddots & \ddots \\ \ddots & -1 & & 2 & -1 & & & & \end{pmatrix}$$

572 of size $(N - 2) \times N$ and hence the constant and linear components of the solution are not damped in the
573 Tikhonov regularization (5).

574

575 **Appendix 2: comparison of 1D and higher dimensional models for SSB**

576 In order to ascertain the effect of the terrain geometry we conducted a number of forward simulations
577 with the model (1) using as boundary data the synthetic GST shown in Fig 4 (dashed line) and already
578 employed for the sensitivity analysis.

579 First we computed the solution of the one-dimensional model (1). Next we computed the solution of the
580 corresponding three-dimensional model in a computational domain of 400X400 m centred around SBB and
581 500 m deep, whose the top surface was obtained from a DEM (with a resolution of 10m . Such domain was
582 discretized with the GMSH program and the heat equation was solved using linear Lagrange finite elements
583 in space and backward Euler in time. The mesh was refined until numerical convergence was observed and
584 in Figure 14 we present the results for a mesh with 1.3 million of tetrahedra. The numerical simulations
585 were performed with the HPC cluster of the Dipartimento di Matematica of the Università di Torino.

586 Figure 14 compares the temperature anomalies that each of the models would predict at SSB at present
587 time. The red dots are the predicted well anomalies at the depth of the thermometers at SSB. One can see
588 that the predictions of the two-dimensional model with flat terrain (blue line) almost coincide with those of
589 the one-dimensional one. Furthermore, the two-dimensional model applied to the section with the steeper
590 sides (the SSW-NNE one, orange line) gives rise to predictions that are within the instrumental error
591 ($\pm 0.1^\circ\text{C}$) whereas the N-S section (red line), which has a flatter terrain, gives rise to predictions that are
592 quite close to those of the one-dimensional model. The predictions of the 3D model (dashed black line) are
593 very close to the 2D flat and the 2D N-S (with difference always $< 0.03^\circ\text{C}$).

594 Finally, let us remark that for the forward model, a numerical 3D simulation takes hours to complete on 16
595 computing nodes of our HPC cluster. Using a numerical multi-dimensional simulator in the inverse problem
596 would of course require to compute several times the forward model and would thus take a lot longer than
597 the few seconds in which our proposed method can compute the reconstructed GST depicted in Fig. 10.

598

599

600

601

602

603

604

605

606

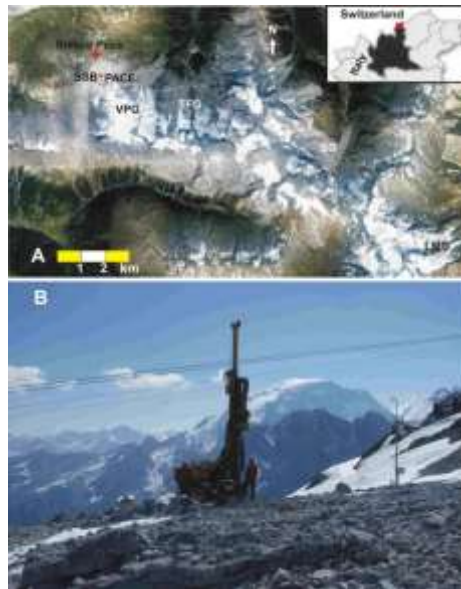
607

608

609

610

Fig. 1



611

612

613

614

615

616

617

618

619

620

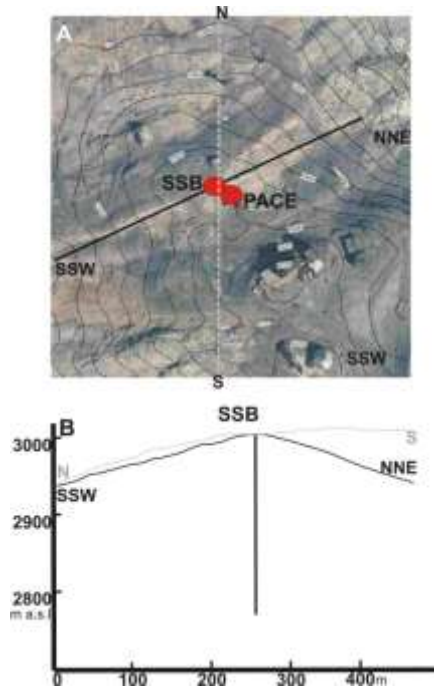
621

622

623

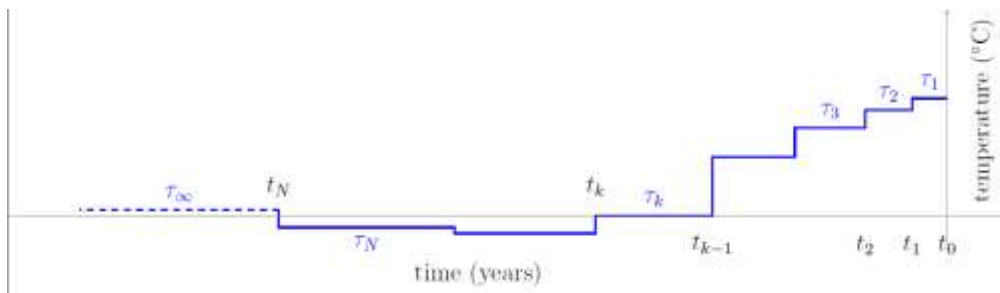
624

Fig. 2



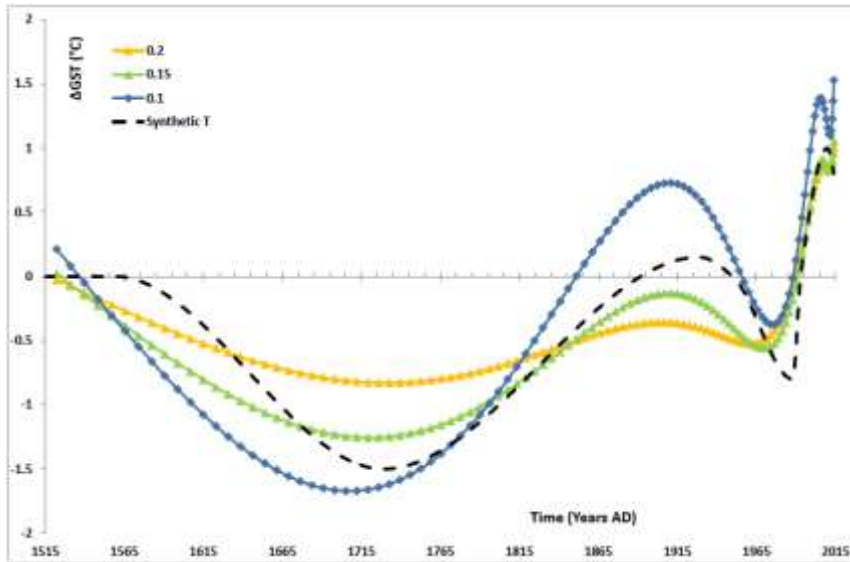
625
626
627
628

Fig.3



629
630
631
632
633
634
635
636
637
638
639

Fig.4

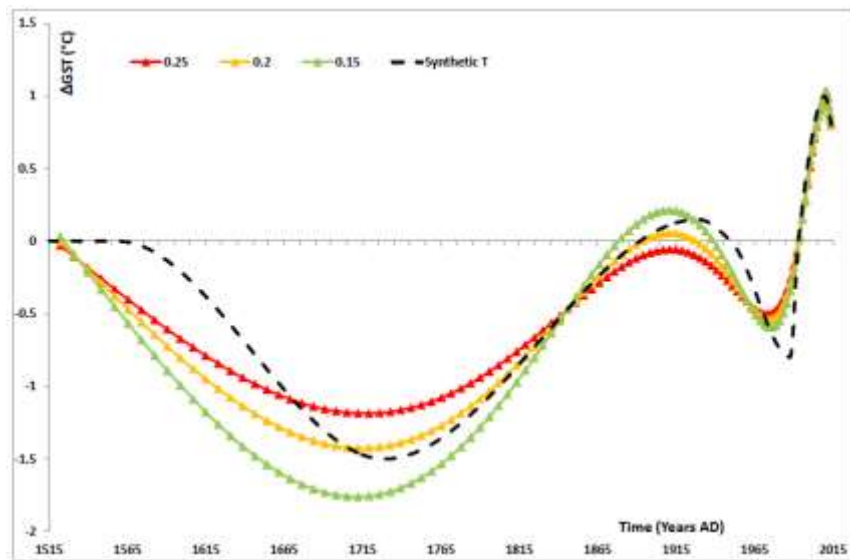


640

641

642

Fig. 5



643

644

645

646

647

648

649

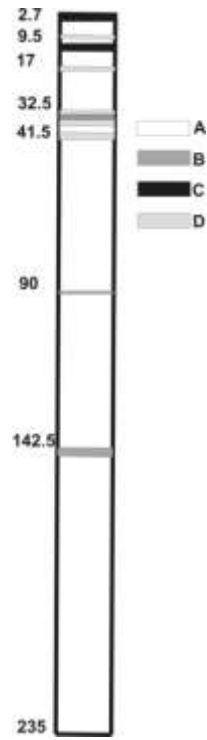
650

651

652

653

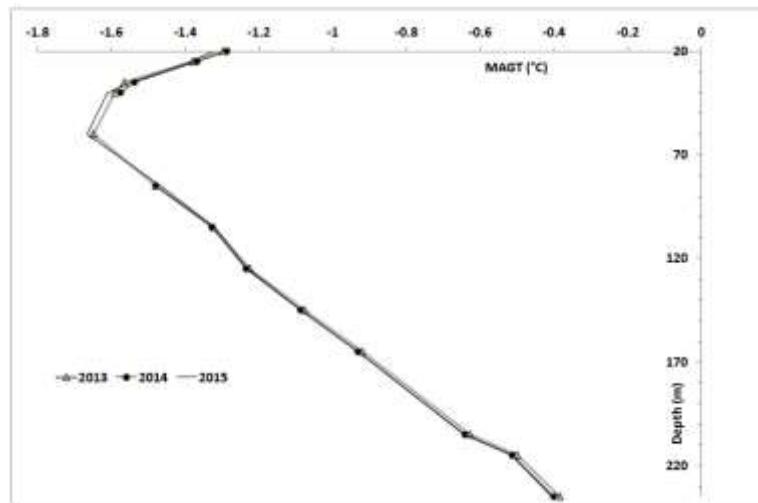
Fig. 6



654

655

Fig. 7



656

657

658

659

660

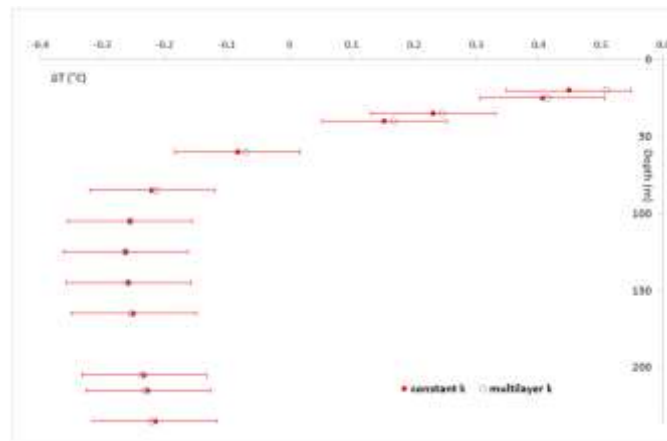
661

662

663

664

Fig. 8



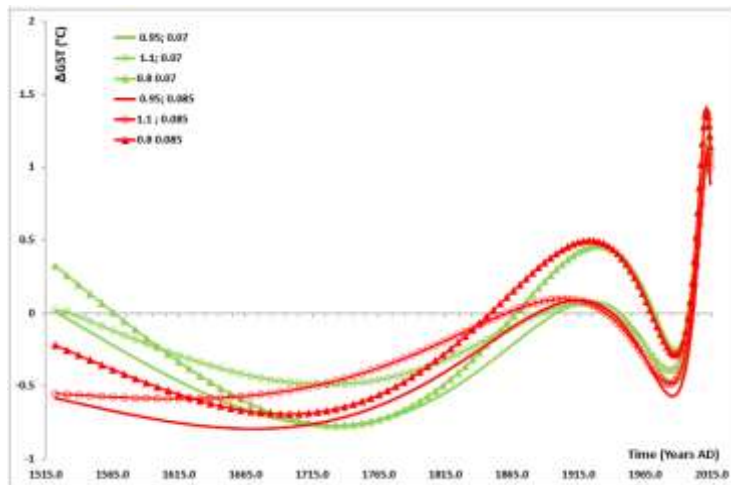
665

666

667

668

Fig. 9



669

670

671

672

673

674

675

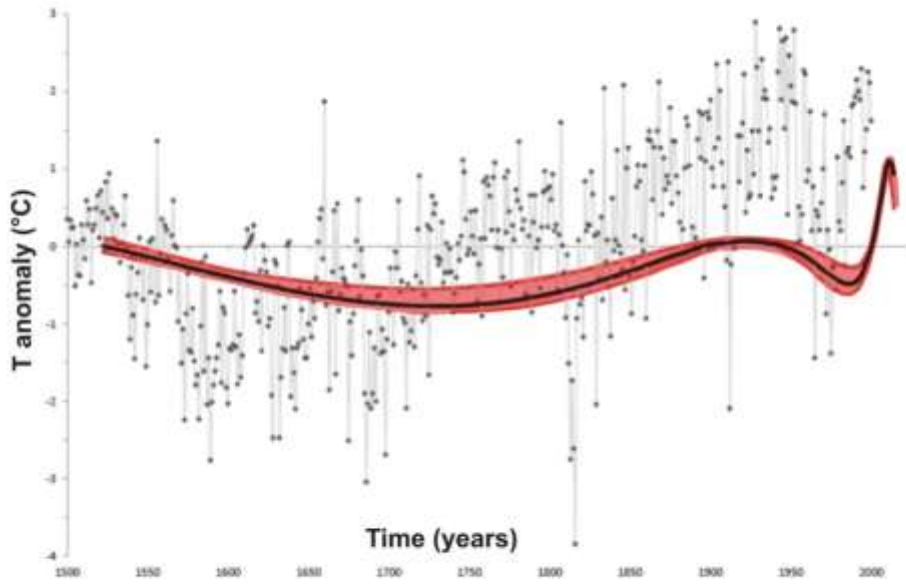
676

677

678

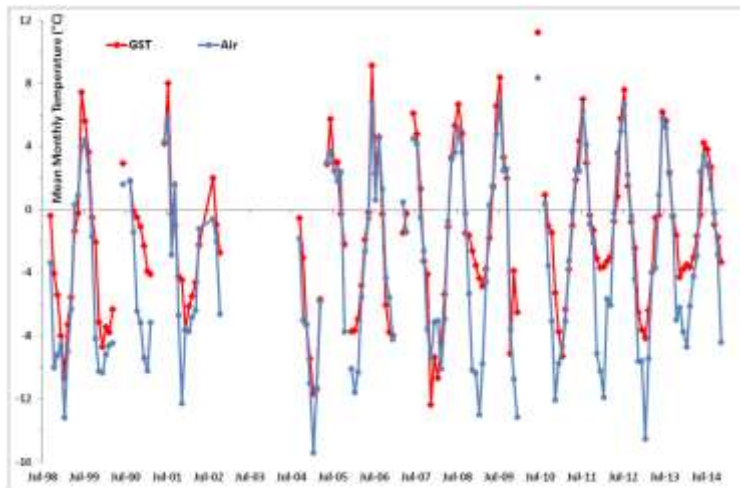
Fig. 10

679
680
681



682
683
684

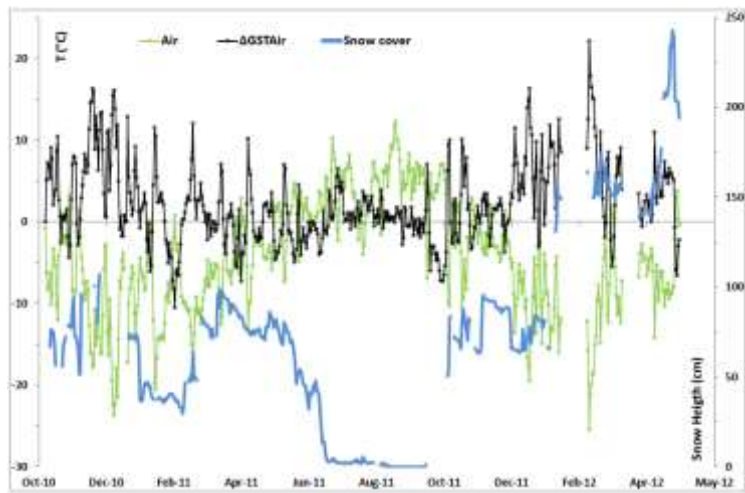
Fig. 11



685
686
687
688

Fig. 12

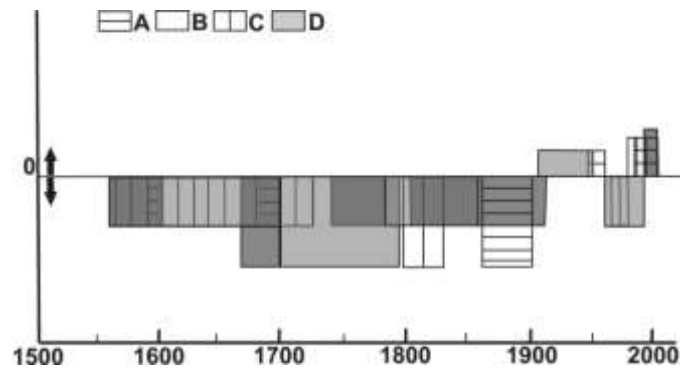
689



690

691

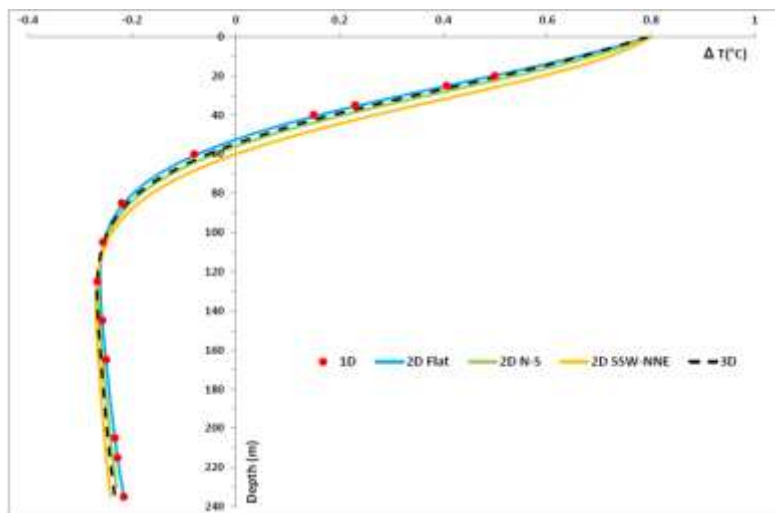
Fig. 13



692

693

Fig. 14



694

695